Graphene-Assisted Controlled Growth of Highly Aligned ZnO Nanorods and Nanoribbons: Growth Mechanism and Photoluminescence Properties

Ravi K. Biroju,[†] P. K. Giri,[*,†,‡] Soumen Dhara,[‡] Kenji Imakita,[‡] and Minoru Fujii[‡]

[†]Centre for Nanotechnology, Indian Institute of Technology Guwahati, Guwahati 781039, India
[‡]Department of Electrical and Electronic Engineering, Graduate School of Engineering, Kobe University, Kobe 657−8501, Japan

S *Supporting Information*

ABSTRACT: We demonstrate graphene-assisted controlled fabrication of various ZnO 1D nanostructures on the SiO_2/graphene substrate at a low temperature (540 °C) and elucidate the growth mechanism. Monolayer and a few layer graphene prepared by chemical vapor deposition (CVD) and subsequently coated with a thin Au layer followed by rapid thermal annealing is shown to result in highly aligned wurtzite ZnO nanorods (NRs) with clear hexagonal facets. On the other hand, direct growth on CVD graphene without a Au catalyst layer resulted in a randomly oriented growth of dense ZnO nanoribbons (NRBs). The role of in-plane defects and preferential clustering of Au atoms on the defect sites of graphene on the growth of highly aligned ZnO NRs/nanowires (NWs) on graphene was established from micro-Raman and high-resolution transmission electron microscopy analyses. Further, we demonstrate strong UV and visible photoluminescence (PL) from the as-grown and post-growth annealed ZnO NRs, NWs, and NRBs, and the origin of the PL emission is correlated well with the X-ray photoelectron spectroscopy analysis. Our results hint toward an epitaxial growth of aligned ZnO NRs on graphene by a vapor−liquid−solid mechanism and establish the importance of defect engineering in graphene for controlled fabrication of graphene−semiconductor NW hybrids with improved optoelectronic functionalities.

KEYWORDS: *graphene−semiconductor hybrid, ZnO nanowires, chemical vapor deposition, rapid thermal annealing, photoluminescence, defect engineering*
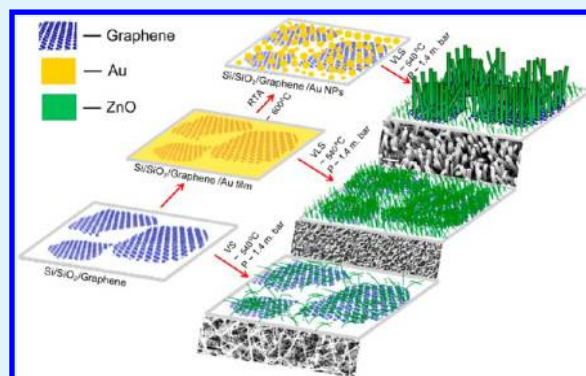
1. INTRODUCTION

The absence of a band gap in graphene and its remarkable electronic and optical properties foster the fabrication of plenty of 2D−1D integrated semiconductor hybrid nanostructures.[1] In such a kind of graphene-based hybrid structure, graphene acts as the 2D substrate onto which several 1D semiconducting nanomaterials can be grown and superior properties may be expected. Graphene-mediated growth of semiconducting nanowire (NW) and nanorod (NR) heterostructures has received enormous attention for possible integration of 1D and 2D nanomaterials yielding superior electronic and optoelectronic functionalities. The presence of a graphene layer over a dielectric surface may catalyze the growth of well-aligned NWs. The extraordinary properties of graphene, such as the presence of 2D hexagonal sheet-like structure having one atom thick sp^2-hybridized carbon,[2] high carrier mobility, excellent optical transparency (97.7%) over the entire visible region,[3] flexibility,[4] and high thermal conductivity,[5,6] make it an attractive candidate to integrate with semiconducting NWs, NRs, and nanoribbons (NRBs) that may exhibit exceptional properties. It is expected that integration of the highly conductive graphene and extreme

photosensitivity of the semiconducting NWs could improve the optical characteristics of graphene−semiconducting NW based hybrid structures as compared to the semiconducting NWs only.[7,8] Thus, it can serve as an exciting active material in the field of photovoltaic and optoelectronic device applications. In the process of fabrication of NW heterostructure, researchers utilized different kinds of heterostructure architectures using various suitable external materials including graphene.[7,9−13]

Among the graphene-based 2D−1D hybrid structures, fabrication of vertically aligned semiconductor NRs and NWs onto the graphene layer has received considerable attention[1,14−16] to develop unconventional sophisticated optoelectronic and photonic devices in the form of flexible and transparent electronic devices. Graphene-assisted controlled growth of ZnO nanostructures is little explored in the literature, and therefore the growth mechanism is not understood well. Epitaxial growth of vertical semiconductor NWs on graphitic

substrates has been demonstrated recently by Munshi et al.[14] It was proposed that due to close matching of hexagonal ZnO with certain atomic configurations of graphene epitaxial growth of ZnO NWs on graphene is quite likely. However, there is no experimental evidence available yet in support of this hypothesis. Ng et al.[17] reported fabrication of vertically aligned 2D and 1D ZnO nanostructures on electrically conducting highly oriented pyrolytic graphite (HOPG) and on insulating (1120) sapphire substrates using a carbothermal reduction process and Au as a catalyst. This process involved reaction at relatively high temperature (900 °C). The choice of substrate including a buffer layer and a metal catalyst layer is among the important factors determining the orientation of the NWs in thermal vapor deposition growth. Vertical growth of ZnO NWs on conducting substrates, e.g., Cu, stainless steel alloys,[18] and improved electrical and thermal conductivity for resistive-switching random access memory device applications were reported.[19] The graphene and graphene−metal hybrid as buffer layers on a Si/SiO$_2$ substrate may help to control the density and orientation of the ZnO NWs/NRs. The high optical transparency and superior electronic properties of graphene make it a material of choice for a wide range of applications in optoelectronic and photonic devices. Kim et al.[20] demonstrated the synthesis of vertically aligned ZnO nanoneedles and nanowalls on few layer graphene sheets by sophisticated metal oxide chemical vapor deposition and studied its photoluminescence (PL) characteristics. To date, most of the graphene-based ZnO hybrid structures were fabricated by solution processes.[7,21−26] There are very few reports on the growth of vertically aligned, high density, and high aspect ratio graphene−ZnO hybrid nanostructures using a thermal vapor deposition technique that is compatible with the fabrication of integrated optoelectronic devices.[15,27] Note that some of the earlier reports adopted extremely high growth temperatures, and the detailed optical characterization of the resulting nanostructures was lacking. Further, the mechanism of growth was not understood well. It is imperative to understand the growth mechanism to achieve precise control over morphology and structure of the resulting nanostructures.

In this article, we demonstrate the graphene-assisted controlled growth of different ZnO nanostructures on single layer and few layer graphene substrates at 540 °C using a thermal vapor deposition technique. The morphology and orientation of the ZnO 1D nanostructures on graphene are controlled by changing the pretreatment conditions on the graphene substrate. The individual and combined effects of graphene layer and Au catalyst on the structure and quality of the graphene−ZnO hybrid structures are studied systematically, and the growth mechanism is elucidated based on the experimental observations. Optical properties of the graphene−ZnO hybrid structures are studied by PL spectroscopy, and the origin of the PL bands is found to correlate well with the X-ray photoelectron spectroscopy (XPS) analyses.

2. EXPERIMENTAL SECTION

2.1. Synthesis of Graphene. To synthesize the graphene layer, high purity copper foil of thickness 25 μm (Alfa−Aesar) was used as a substrate. First, a piece of Cu foil was inserted into the quartz chamber inside a thermal chemical vapor deposition (CVD) system developed in-house, and the chamber was evacuated to a vacuum of 4×10^{-4} mbar. Subsequently, the inserted Cu foil was preannealed in reduced environment at 1000 °C by flowing 200 sccm (standard cubic centimeters per minute) H$_2$ gas for 30 min. Finally, the reaction was carried out at a temperature of 1000 °C and pressure of 4.0 mbar with

controlled flow of CH$_4$ (18 sccm) and H$_2$ (200 sccm) for 30 min. Since graphene was deposited on both sides of the Cu foil, the back side graphene was removed by diamond polishing. On the front side, poly(methyl methacrylate) (PMMA)/toluene was spin coated on the graphene, and then the underlying Cu was etched in Fe(NO$_3$)$_3$ solution. PMMA/graphene floating on the Fe(NO$_3$)$_3$ solution was rinsed in the deionized (DI) water a few times until the PMMA and metal impurities were removed. Subsequently, it was transferred to Si/SiO$_2$ substrate and dried.

2.2. Fabrication of ZnO Nanostructures on the Graphene Substrate. Various kinds of ZnO nanostructures were grown on the above-prepared graphene substrates by using a thermal vapor deposition system for different pretreated substrates. At first, ∼5 nm thick Au film was deposited on the graphene substrate and bare oxidized Si (Si/SiO$_2$) substrate by radio frequency magnetron sputtering. Some of the Au-coated substrates were treated by rapid thermal annealing (RTA) at 600 °C in Ar atmosphere to form Au islands. For the growth of ZnO nanostructures, commercial activated zinc powder (purity ∼99%, Aldrich) was taken as a source material in an alumina boat and placed at the center of a horizontal quartz tube, and the assembly was inserted inside a horizontal muffle furnace. The Au-coated graphene substrates with or without RTA treatment were placed downstream ∼5 cm away from the source. Initially, the quartz chamber was pumped to a pressure of ∼10^{-3} mbar. The source temperature was kept at ∼550 °C, and substrate temperature was ∼540 °C. Throughout the temperature ramp 300 sccm of Ar gas was flushed until it reached the set point with a heating rate of 18 °C/min to prevent the oxidation of the graphene. When the furnace reached the source temperature (550 °C), 20 sccm of O$_2$ gas was introduced, and the gas pressure inside the chamber was maintained at 1.4 mbar for the growth time of 50 min. After the completion of the reaction, the furnace was cooled to room temperature. ZnO deposition was carried out on four different sets of substrates under identical growth conditions as described in Table 1. To improve the crystalline quality

Table 1. Details of the Substrate Pretreatment Conditions and Morphology of the Resulting ZnO Nanostructures on Different Substrates

sample code	substrate and pretreatment	ZnO nanostructures
GRZN1	Si/SiO$_2$/graphene/Au, RTA	NRs, aligned, hexagonal
GRZN2	Si/SiO$_2$/graphene/Au	NWs, aligned
GRZN3	Si/SiO$_2$/graphene	NRbs, random
ZN3	Si/SiO$_2$/Au, RTA	NWs, random

of as-grown graphene−ZnO hybrid nanostructures, we performed post-growth annealing at 500 and 700 °C in an Ar atmosphere (50 sccm flow) for 1 h and studied the resulting structural and PL properties.

2.3. Characterization. The morphology and crystal structure of the as-grown samples were characterized by using field emission scanning electron microscope (FESEM, Sigma, Zeiss), high-resolution transmission electron microscopy (HRTEM, JEM2100 operated at 200 kV, JEOL), and an X-ray diffractometer (XRD) (Rigaku RINT 2500 TRAX− III, Cu Kα radiation). Micro-Raman measurements were performed using a high-resolution Raman spectrometer (HORIBA Lab Ram HR 800), with excitation source 514.5 nm (Ar$^+$ ion laser), to examine the quality and number of layers of graphene. The steady state PL spectra of all the samples were recorded with a 325 nm He−Cd laser excitation using a commercial PL spectrometer (Fluorolog-3, Horiba) equipped with a photomultiplier tube detector. To compare the PL results, all the as-grown and annealed samples were measured under identical conditions. XPS measurements were carried out with a fully automated XPS microprobe (PHI-Xtool, Ulvac-Phi) using an Al Kα X-ray beam (1486.7 eV). The carbon 1s spectrum was used for the calibration of the XPS spectra recorded for various samples.

3. RESULTS AND DISCUSSION

As-synthesized (CVD grown) graphene samples were first characterized by Raman spectroscopy and electron microscopy before fabricating the graphene−ZnO hybrid nanostructures. Figure 1(a) shows the Raman spectra at different spots of the
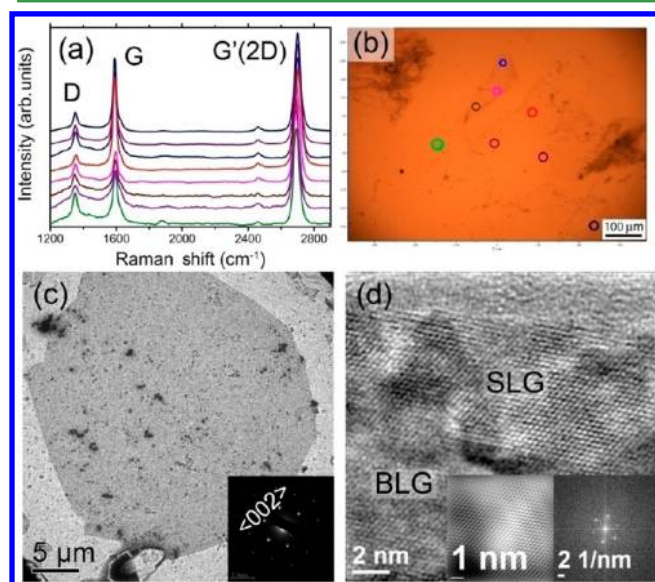

Figure 1. (a) Raman fingerprints of as-synthesized graphene transferred to Si/SiO$_2$ substrate measured with the excitation wavelength of 514.5 nm and (b) corresponding scanning positions marked in the optical microscope. (c) TEM image of the graphene layer after transferring onto a TEM grid with the corresponding SAED pattern as an inset. (d) HRTEM image of SLG and BLG; inset shows the IFFT and FFT images of the hexagonal lattice spots.

as-synthesized graphene transferred onto a Si/SiO$_2$ (300 nm) substrate. Corresponding scanning positions are shown by markers in the optical microscope image in Figure 1(b). The

sharp intense Raman mode at ∼2700 cm^{-1}, so-called G′(2D) band, is a fingerprint of graphene, and the graphitic G band at ∼1590 cm^{-1} signifies the sp^2 hybridization of carbon atoms covalently bonded and assigned to the E$_{2g}$ mode of in-plane C−C stretching vibration.[28] The D band at ∼1352 cm^{-1} is relatively weak, and it can be ascribed to defects such as point, edge, and line defects, as confirmed from the HRTEM analyses discussed later. Raman line shape analysis shows that the graphene substrates that are used for the fabrication of ZnO nanostructures are 90% monolayer graphene. Crystalline quality of the graphene was investigated by transmission electron microscopy (TEM). Figure 1(c) shows the low-resolution TEM image of the graphene layer, and the inset represents the corresponding selected area electron diffraction (SAED) pattern that confirms the hexagonal diffraction patterns of the single-crystalline graphene layer. The HRTEM image of the graphene layer (Figure 1(d)) clearly shows the hexagonal lattice fringes of the single (SLG) and bilayer graphene (BLG), and the inset depicts the inverse fast Fourier transform (IFFT) and fast Fourier transform (FFT) images of a nearly defect-free single layer of carbon atoms and one atom thickness, respectively.

A systematic study on the individual role of graphene and Au catalyst and the effect of graphene−Au film and graphene−Au NP hybrids was carried out to elucidate the growth mechanism of various ZnO nanostructures. In the following subsections, we present each of these cases systematically.

3.1. Effect of Graphene Layer and Graphene−Au Film.
Figure 2 illustrates the individual role of graphene and Au layers in the formation of ZnO NWs and NRBs on the graphene substrate. Figure 2(a) shows a low-resolution FESEM image of ZnO nanostructures grown on the graphene with/without Au layers formed by masking with a copper grid (used in TEM) while depositing the Au film. The regions I and II with bright and dark contrasts refer to the absence and presence of Au coating on the graphene layer, respectively. Region III refers to a transition region between regions I and II. Figure 2(b) and its
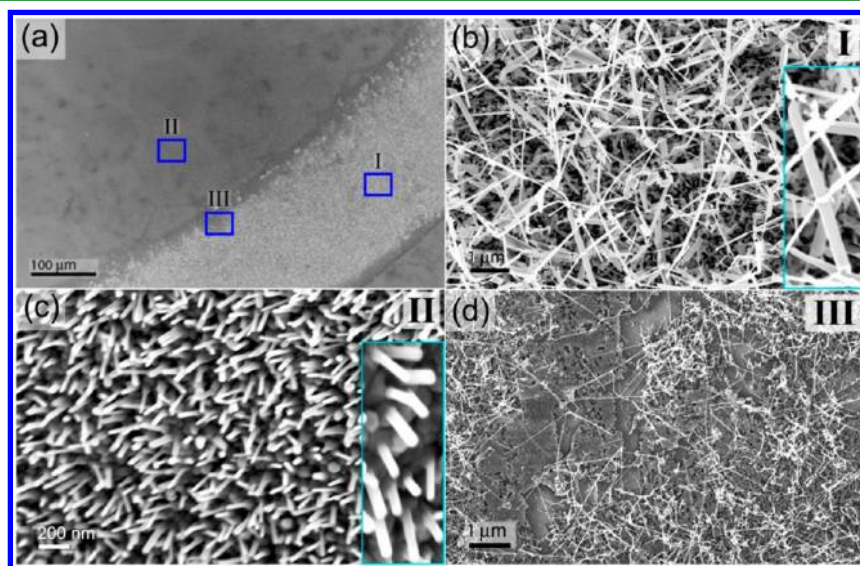

Figure 2. (a) FESEM image of ZnO NWs/NRBs grown on the Si/SiO$_2$/graphene/Au film; regions I and II with bright and dark contrast refer to a graphene layer without and with Au film, respectively. Region III refers to the transition region between region I and II. (b,c) Magnified view of regions I and II depicting the growth of randomly oriented ZnO NRBs and aligned ZnO NWs, respectively. Inset in (b) and (c) shows higher-magnification images of the NRBs and NWs, respectively. (d) Magnified view of region III showing nonuniform growth of ZnO NRBs in the absence of a Au layer.
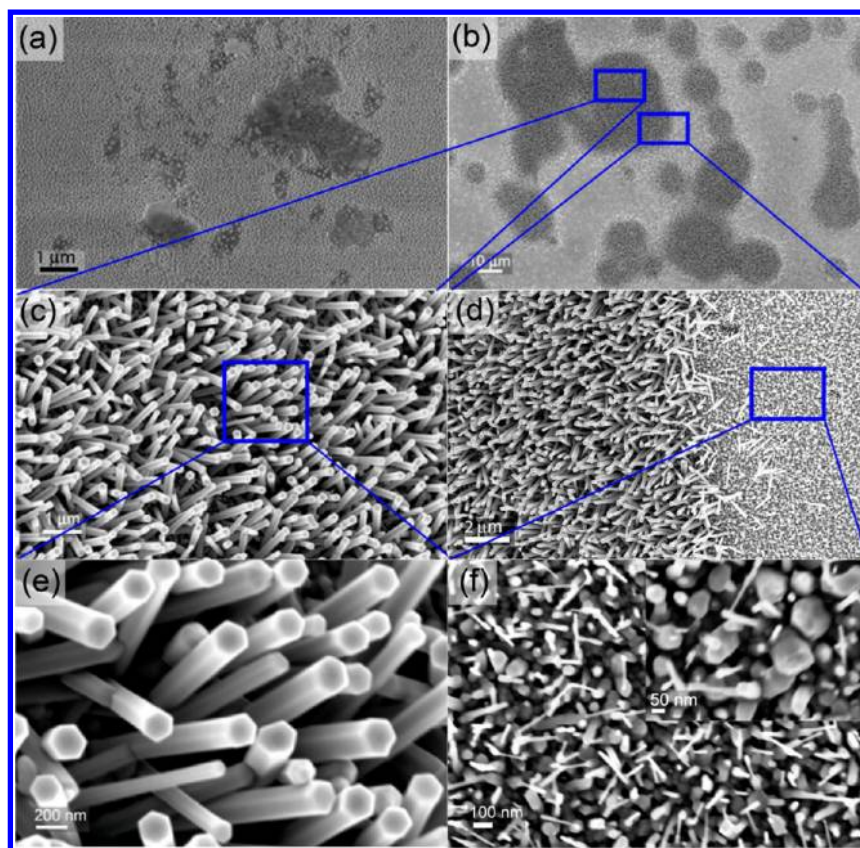
Figure 3. FESEM images of Si/SiO$_2$/graphene/Au NP (RTA-treated) substrates (a) before and (b) after the growth of ZnO NRs. The region with dark (bright) contrast refers to the presence (absence) of a graphene layer. (c) Magnified view of the portions of (b) with the graphene layer marked with blue boxes; it depicts aligned ZnO NRs (GRZN1) with hexagonal facets formed on the graphene layer. (d) Magnified view of a portion of (b) with and without the graphene layer shown side by side. No clear NRs (without hexagonal facets) are formed in the absence of a graphene layer. (e,f) Represent the magnified view of ZnO nanostructures shown in (c) and (d), respectively. Nonuniform NWs without any hexagonal facets can be seen in the inset of (f).

inset show higher-magnification images of region I, clearly showing randomly oriented and nonuniform ZnO NRBs formed on graphene in the absence of the Au layer. In contrast, a dense and nearly aligned array of ZnO NWs is formed in the case of a graphene−Au film layer (region II), as shown in Figure 2(c). The inset of Figure 2(c) shows a higher-magnification image of the ZnO NWs that clearly reveals the absence of any hexagonal faceted NWs. Figure 2(d) shows the magnified view of the FESEM image of ZnO NRBs grown on region III. In region III, the density of the NRBs is lower than that of region I, due to the finite thickness and rough edge of the mask that reduces the nucleation sites for the growth of the ZnO NRBs. Thus, Au catalyst plays a crucial role in the growth and vertical alignment of the ZnO NWs on the graphene substrate. The critical role of Au catalyst in the vertical growth of ZnO NWs on the usually employed dielectric surface has been extensively studied. It will be evident from the discussion below that in the present case the underlying graphene layer plays a crucial role in the growth of the aligned ZnO NWs.

3.2. Effect of Graphene−Au NPs (RTA Treated). Figure 3(a) and (b) shows the low-resolution FESEM images of the RTA-treated graphene/Au substrate before and after the growth of ZnO NRs, respectively. Regions with dark contrast in the images refer to the coverage of graphene. Figure 3(c) and 3(d) shows the magnified view of the respective regions with graphene/Au NPs and the transition region due to the mask edge. The vertical alignment and hexagonal facets of ZnO NRs

are clearly seen by the morphological features. Interestingly, in the presence of the graphene−Au NP layer, dense ZnO NRs with clear hexagonal facets are formed at 540 °C. The growth of aligned ZnO NRs and NWs on graphene at this temperature is significant, and it establishes the important role of graphene in the low-temperature vapor-phase growth of ZnO NR hybrids with clear hexagonal facets. Figure 3(e) and 3(f) shows the magnified view of the images shown in Figure 3(c) and 3(d). Figure 3(f) along with its inset depicts that randomly oriented ZnO NWs/NRs are formed even in the presence of Au catalyst NPs (RTA treated) on the Si/SiO$_2$ substrate without the graphene layer. Further, these NRs/NWs do not possess hexagonal facets, as shown in the inset of Figure 3(f). Morphological analysis revealed that the ZnO NRs shown in Figure 3(e) have clear hexagonal facets and are vertically aligned with an average diameter of ∼150 ± 50 nm and length of ∼2 μm, yielding a high aspect ratio of 12 ± 2. Dark spots on the top face of the ZnO NRs refer to the presence of Au catalyst particles, and this implies a vapor−liquid−solid (VLS) growth mechanism taking place for the ZnO NW growth.

It may be noted that due to the relatively lower-temperature (540 °C) growth adopted here neither Au catalyst nor graphene layer alone on a Si/SiO$_2$ substrate yields aligned ZnO NRs/NWs, as shown in Figure 2(b) and 3(f), respectively. This demonstrates the superiority of the graphene−Au hybrid catalyst over conventionally used Au catalyst for the fabrication of vertically aligned ZnO nanostructures, such as ZnO NRs and
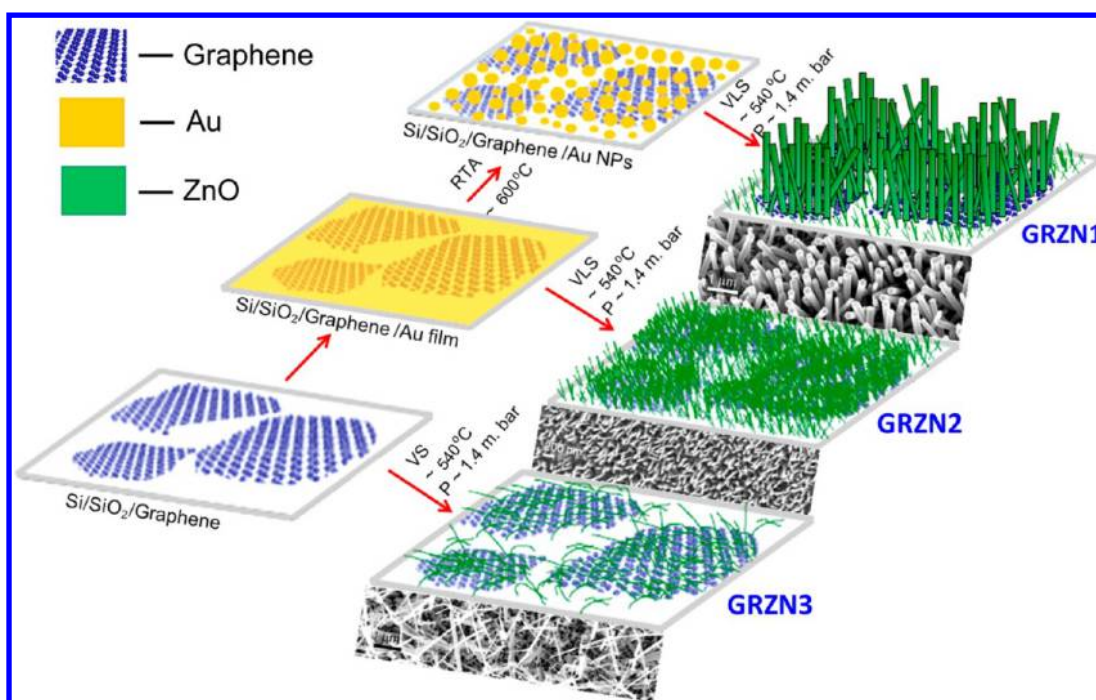
Figure 4. Schematic of the growth processes and resulting morphology of graphene−ZnO hybrid NRs (GRZN1), NWs (GRZN2), and NRBs (GRZN3) for different substrate configurations grown by thermal vapor deposition.

NWs. By controlling the interaction between graphene−Au film and graphene−Au NPs through appropriate pretreatment conditions, it has been possible to control the morphology and orientations of the ZnO nanostructures. The areal density of NRs and NWs in the GRZN1 and GRZN2 samples is ∼1.4 × 10^9 and ∼8.4 × 10^9 cm^{-2}, respectively, which are larger than the earlier reports.[20,27] The areal density was estimated by manual counting of the average number of NWs and NRs existing within a certain area of the FESEM images at different portions. The upper portion of some of the aligned NRs looks slightly bent which may be due to fluctuations in the flow of carrier gas.

3.3. Direct Growth on Si/SiO$_2$ and Si/SiO$_2$/Au NPs without a Graphene Layer. In the absence of a graphene layer, the direct growth of ZnO nanostructures on the Si/SiO$_2$ substrate yielded ZnO nanotetrapod-like structures with very small diameter and length in the range of 200−300 nm, as shown in Figure S1 (Supporting Information). However, the growth on Si/SiO$_2$/Au NP (RTA-treated Au film) substrates yielded randomly oriented dense ZnO NRs/NWs as discussed earlier (see Figure 3(f)). It may be noted that no aligned NRs/NWs are formed on these substrates at the present growth temperature. In essence, the relationship between substrate pretreatment conditions and the morphology of the ZnO nanostructures can be summarized by a schematic shown in Figure 4. This emphasizes the importance of graphene in the self-assembly of Au NPs on it and the graphene−Au NP hybrids as a versatile platform for the fabrication of aligned ZnO NRs with hexagonal facets.

Figure 5(a) and (b) represents the low-resolution and high-resolution TEM images of the graphene−ZnO NW hybrids (GRZN2), respectively. The HRTEM image clearly reveals the single crystalline lattice fringes of the ZnO NW. The IFFT image shown in the inset reveals a d-spacing of 2.58 Å that is consistent with the strong XRD peak at 34.6° from the (002) plane of the ZnO NR/NW. Figure 5(c) shows the XRD pattern
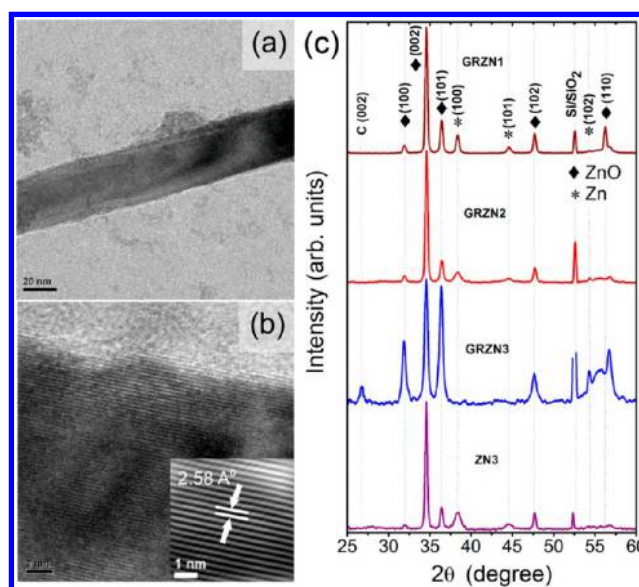

Figure 5. (a) TEM images of graphene−ZnO NWs in GRZN2 and (b) corresponding HRTEM image depicting the clear lattice fringe for the ZnO ⟨002⟩ plane with its d-spacing shown as an inset. (c) XRD patterns showing c-axis orientation of the graphene−ZnO hybrid nanostructures for different substrates.

of the as-grown ZnO NRs (GRZN1), NWs (GRZN2), NRBs (GRZN3) on graphene, and ZnO NWs on graphene-free Si/SiO$_2$/Au substrate (ZN3). The intensity of the XRD peak at 34.6° from the (002) plane is high for GRZN1, GRZN2, and ZN3 as compared to that of GRZN3. This implies that the majority of NRs and NWs is (002) or c-axis oriented. In the case of GRZN3, peaks at 32° (100) and 36.36° (101) are prominent and reveal random orientations of NRBs, and this is consistent with the FESEM analysis. The weak carbon (002) peak at 26° in the sample GRZN3 originates from the few layer
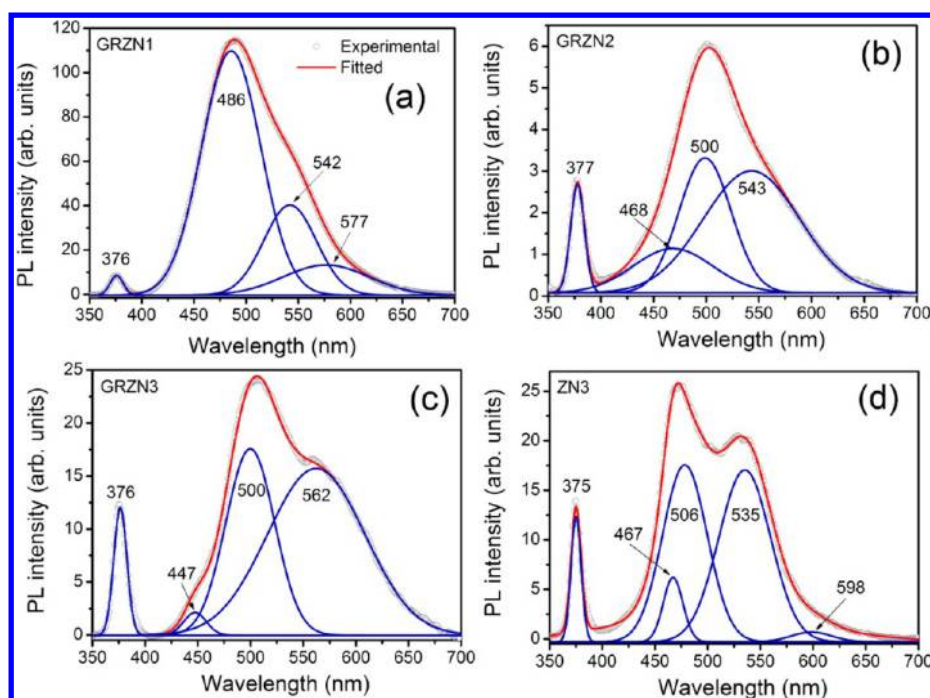
Figure 6. Room-temperature PL spectra of graphene–ZnO hybrid nanostructrues: (a) GRZN1, (b) GRZN2, (c) GRZN3 grown on graphene layer, and (d) ZnO NWs grown without graphene layer (ZN3). Solid blue lines are the Gaussian curves fitted to the experimental data (symbols).

graphene and is due to partial coverage of the ZnO NRBs on the substrate, while the absence of this peak in GRZN1 and GRZN2 samples implies a full coverage of the ZnO NRs and NWs on the graphene substrate such that the graphene signal is below the detection limit. Some of the secondary peaks at 38.37° (100), 44.58° (101), and 54.3° (102) arise from residual Zn metal nanoparticles, perhaps due to the low-temperature growth process adopted here. The sharp peak at 52.6° (002) arises from the single crystalline Si substrate.

3.4. Photoluminescence Studies. Optical properties of the as-grown and post-growth annealed (500 °C in Ar gas atmosphere) graphene–ZnO nanostructures were investigated by PL spectroscopy. Figure 6 represents the room-temperature PL spectra of GRZN1, GRZN2, GRZN3, and ZN3 with 325 nm laser excitation. The symbols refer to the experimental data, and the solid lines refer to the Gaussian peaks fitted with the experimental data. In each case, the UV peak at ∼375 nm is due to the near band edge (NBE) emission, and the broad visible band centered at ∼500 nm arises from the defects in ZnO nanostructures. Due to the asymmetry in the PL spectra, multiple peaks are fitted with Gaussian line shape, and Table T1 (Supporting Information) summarizes the peak parameters extracted from the fitting for each sample before and after annealing. The possible identities of each peak are also mentioned in Table T1 (Supporting Information), based on our observations and the literature reports. The sharp NBE peak varying between 375 and 378 nm is significant in all the samples, and it is due to the free excitonic transition. The intensity of the UV peak is nearly equal in GRZN1, GRZN3, and ZN3, while it is about 5 times lower in GRZN2. On the other hand, the visible band is strongest in GRZN1 and weakest in GRZN2. Note that the center of the visible PL peaks differs from sample to sample, though the UV peak position remains unchanged. A strong and sharp UV peak in these samples indicates reasonably good crystalline quality of the as-grown ZnO NRs, NWs, and NRBs. The broad peak in the visible

region is well-known for the intrinsic defects in ZnO, such as oxygen vacancies (V_o),[29] deep interstitials of oxygen (O_i),[30] or Zn (Zn_i) and antisite oxygen (O_{Zn})[31,32] that may be formed on the surface of the ZnO nanostructures during the growth process. In the as-grown ZnO nanostructures, several green and yellow emissions were identified at different wavelengths, as shown in Table T1 (Supporting Information). In the present case, the samples were grown at a relatively low substrate temperature (540 °C) with a Zn source in the presence of oxygen flow. The EDX analysis shows that atomic percentage of Zn is nearly half that of the oxygen. This is consistent with the XPS analysis presented later. Thus, O_i and V_{Zn} are more likely to be present in these samples, contrary to the usually reported V_o defects in ZnO nanostructures.

Interestingly, recent calculation predicts that the formation energy sequence of defects in ZnO is $V_{Zn} < O_i < O_{Zn} < V_o$ at low growth temperatures.[32] On the basis of the earlier reports and the XPS analysis on the ZnO NWs/NRs, the PL peak arising in the range 447–468 nm in different samples may be attributed to the doubly ionized Zn vacancies (V_{Zn}^{2-}).[31,32] Note that the as-grown GRZN1 does not exhibit this peak. The PL peak observed in the range 483–506 nm is the commonly observed green emission from the vapor-deposited ZnO NWs. Theoretical calculation on the defect formation of ZnO shows that the origin of strong green emission is likely to be either V_o or V_{Zn}.[31,33–35] Most of the previous experimental reports suggested that the origin of this emission could be the recombination of photogenerated holes with the electrons belonging to V_o states on the surface of the NWs.[33,36] Thus, the PL peak observed in the range 483–506 nm is tentatively attributed to the V_o states. On the other hand, the PL peaks in the range of 528–543 nm arise from deep level defects, either O_{Zn} or neutral O_i.[30,32,37] Further, the observed yellow emission in the range of 561–598 nm may be attributed to the ionized O_i induced transitions.[37] Note that under the present growth conditions deep interstitial defects are expected in ZnO along
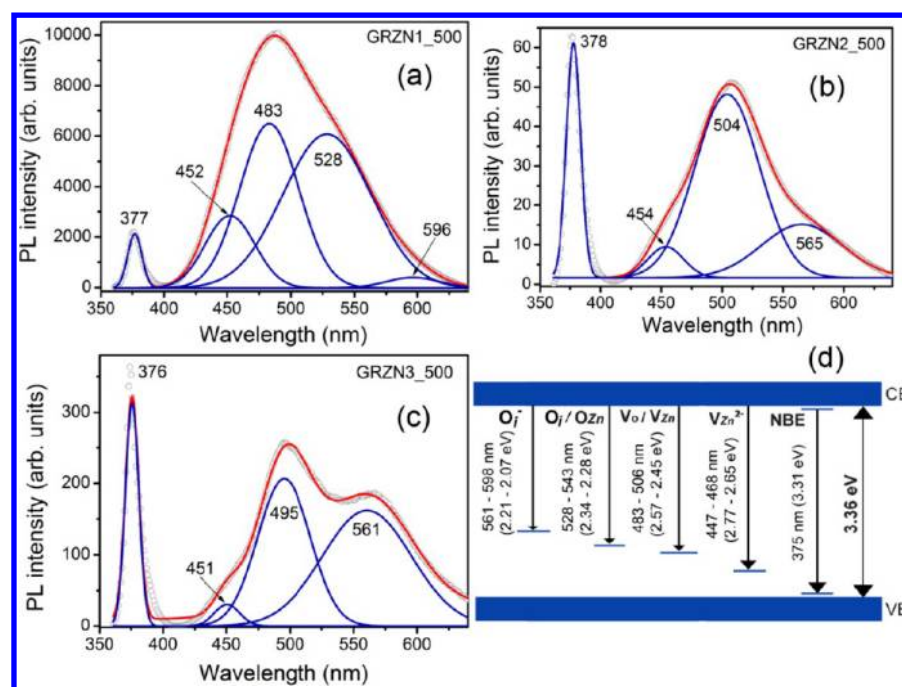
Figure 7. PL spectra of graphene−ZnO hybrid systems after post-growth annealing at 500 °C: (a) NRs (GRZN1_500), (b) NWs (GRZN2_500), and (c) NRBs (GRZN3_500) hybrids. Gaussian fitted peaks are shown with solid lines with peak centers in units of nanometers. (d) Schematic of the band gap defect states tentatively assigned to various PL bands.

with the oxygen vacancy related surface defects. Due to large surface area of the ZnO NWs and NRs, the surface state related visible PL is significant in these samples, despite a good crystalline core as evidenced by the XRD and HRTEM analysis. Willander et al. reported strong UV and visible PL from highly crystalline aligned ZnO NRs grown on p-4H-SiC by the vapor deposition method. They went on to demonstrate white light emitting diodes based on these ZnO NRs.[38] Though there has been debate regarding the origin of various visible peaks in the PL band, it has been suggested that different samples have different defect configurations due to different growth conditions. The peak profile of the defect emission band is dependent on the relative density of the radiative defects. It has been reported that ZnO can exhibit different emissions in the visible range including violet, blue, green, yellow, and orange-red, which are associated with intrinsic and extrinsic defects in the material.[38]

Figure 7(a−c) illustrates the effect of post-growth annealing at 500 °C on the normalized PL spectra of the ZnO nanostructures. The solid lines represent the Gaussian line-shape fittings to the experimental PL spectra. We notice a significant improvement in the intensity of UV as well as visible PL, though no significant shift in the NBE emission occurs after the annealing. In the case of GRZN1, the NBE PL intensity is enhanced by more than 2 orders of magnitude, and the visible PL emission is enhanced by about 2 orders of magnitude after annealing. Figure 7(a) shows that a PL peak appears at 452 nm in GRZN1 after annealing, while it was absent before annealing. In the case of both GRZN2 and GRZN3, the enhancement in UV and visible PL intensity is about 20 and 10 times, respectively. Thus, UV PL intensity is significantly improved by post-growth annealing in all samples indicating improvement in crystalline quality and reduction of nonradiative centers upon annealing. Analysis of PL data further shows that the intensity ratio of the second green emission (483 nm) to UV emission is

reduced by a factor of 4.43 in GRZN1, the third green emission (528 nm) to UV emission is nearly equal, and the yellow emission (596 nm) to UV emission is reduced by a factor of 13.75 after annealing. On the other hand, in GRZN2 and GRZN3, the intensity ratio of both the first and second green emission to UV emission was reduced by a factor of 7.7, 3.0 and 1.3, 1.5, respectively, after annealing. The intensity ratio of yellow emission to UV emission for both these samples is reduced by a factor of 6.2 and 2.8, respectively. Thus, reduction of surface defect density after post-growth annealing is more prominent in ZnO NWs and NRBs as compared to the ZnO NRs. However, ZnO NRs in GRZN1 show the strongest UV as well as visible PL after annealing due to activation of more radiative channels than the nonradiative channels. Such strong PL emission from ZnO NRs is highly beneficial for exploitation in UV/visible light emitting and display devices.[38] Recently, Ashok et al. reported size-tunable enhanced visible emission from ZnO quantum dots.[39] Note that an additional PL peak at ~450 nm was observed in GRZN2 and GRZN3 after annealing at 500 °C. Since the Zn to O ratio is nearly 0.5 in all the samples, V_{Zn} is quite likely to be present in our samples. However, more studies are needed to pinpoint the exact origin of different visible PL peaks in the graphene−ZnO hybrid nanostructures. We have found that further annealing at higher temperature (e.g., 700 °C) does not improve the PL characteristics any further, though the crystalline quality improves strongly as revealed from XRD studies (data not shown). It is observed that after 700 °C annealing the intensity ratio of the UV to visible PL band decreases to some extent.

3.5. XPS Studies. To investigate further the local environment and nature of defects in graphene−ZnO NR and NW hybrids, XPS measurements were carried out. Figure 8(a,b) illustrates the collective XPS spectra of GRZN1 and GRZN2 showing the deconvolution of core level peaks of graphene (C 1s) and ZnO (O 1s, Zn 2p). The corresponding
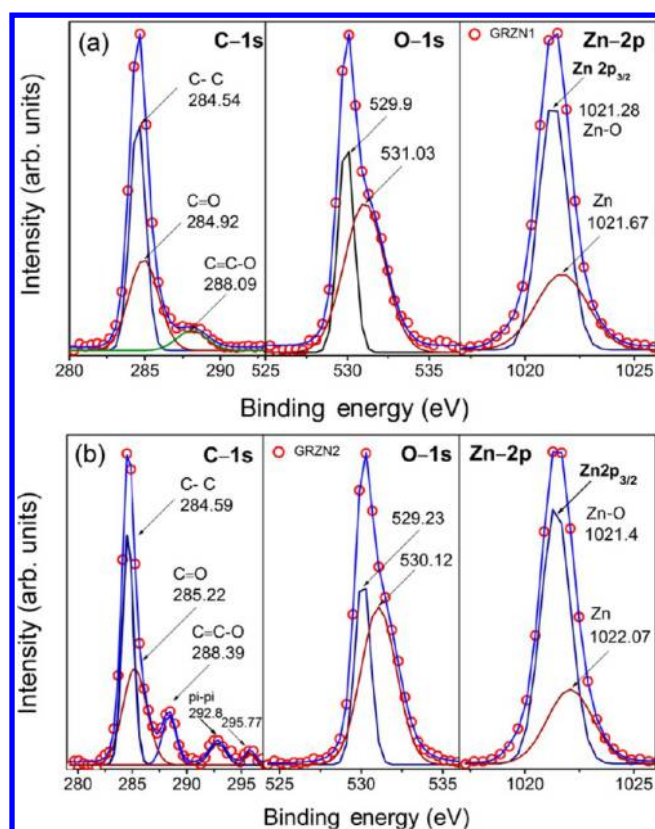
383

dx.doi.org/10.1021/am404411c | ACS Appl. Mater. Interfaces 2014, 6, 377−387

Figure 8. C 1s, O 1s, and Zn 2p core level XPS spectra of various graphene−ZnO nanohybrids: (a) NRs (GRZN1) and (b) NWs (GRZN2) showing the graphene sp^2 C, O, and Zn related peaks with fitted spectra as solid lines and symbols as experimental data. Constituent peaks are marked with binding energy values in units of electronvolts.

parameters are presented in Table 2. The ratio of the relative area of peak 2 to peak 1 in GRZN1 is slightly higher than that in GRZN2; i.e., pure Zn metal in the form of metal nanoparticles and/or Zn interstitials are present in GRZN1. This is fully consistent with the XRD pattern showing diffraction peaks at 38.37° (100), 44.58° (101), and 54.3° (102) (see Figure 5) due to the unreacted Zn metal and the PL spectra showing stronger green emission (higher by 3 orders of magnitude) as compared to the GRZN2, GRZN3, and ZN3. Thus, despite good crystallinity of the ZnO NRs, vertically oriented ZnO NRs shows more surface defects than ZnO NWs and NRBs. This may be due to higher surface area of the hexagonal faceted ZnO NRs than the NRs and NRBs of similar dimensions that contribute to the visible PL. Due to the relatively low growth temperature adopted here, the surface defect density may be high in these samples. Since the PL intensity is strong even after annealing at 500 and 700 °C, the thermal stability of the emitting centers can be considered high. Nevertheless, the strong visible emission from GRZN1 is highly beneficial for practical display application. It would be interesting to investigate the electroluminescence and photovoltaic application of this novel hybrid structure that is a subject of future study.

3.6. Growth Mechanism. To elucidate the growth mechanism of vertically aligned ZnO NRs, NWs, and NRBs, the individual effect of graphene layer and Au catalyst layers was systematically studied by FESEM, HRTEM, and Raman analysis. As shown in the schematic of Figure 4, vertically aligned ZnO NRs with hexagonal facets are formed with the combined effect of graphene and Au NPs. According to an earlier report, there is no formation of ZnO nanowalls even for high density of Au NPs on graphene.[15] The novelty of growing well-aligned ZnO nanostructures on graphene at a lower temperature in our experiment is the substrate conditions that were different from previous studies. In particular, Figure 9(a,b) illustrates the Raman spectra of graphene before and after Au deposition, and corresponding HRTEM images are shown in Figure 9(c,d). From Raman line shape analysis, it is found that the D band intensity is markedly increased, while the G′ (2D) band intensity is reduced after Au deposition. This indicates that defect density in graphene is increased after Au deposition. Upon Au deposition, the change in the G band line shape and down shift in the G′ (2D) band indicates doping of Au atoms in the graphene layer and a tensile strain associated with the doping. With the Au layer on graphene, the high ratio of I_D/I_G = 3.5 and corresponding low interdefect distance[41] L_D = 10.2 nm are significant for the Au clustering at the intrinsic defect sites formed on the graphene surface.[42] This is more evident from the HRTEM images shown with arrows pointing to various kinds of defects in the pristine graphene and graphene/Au hybrid structures, as shown in Figure 9(c,d). In addition, some portions of the pristine graphene substrate show an

fitting parameters are shown in Table 2. The peaks at lower and higher binding energy in the O 1s core level spectrum can be attributed to the oxygen O^{2-} vacancies in the Zn crystal lattice and chemisorbed oxygen,[40] respectively. The lower- and higher-energy components for each sample are shown in Table 2. The relative surface to volume ratio for ZnO NRs is smaller than the NW case. Thus, less chemisorbed oxygen and higher concentration of O_i, O_{Zn}, and V_o are expected in GRZN1 than GRZN2. This is consistent with the PL data that show stronger visible PL in GRZN1 due to the presence of higher O_i, O_i^- and O_{Zn} concentration, while the contribution of V_o and V_{Zn} is significant in GRZN2 and GRZN3 both before and after the annealing. In addition, the deconvolution of the core level peak of Zn $2p_{3/2}$ shows lower and higher binding energy components, as shown in Figure 8. The lower-energy and higher-energy components in each sample represent Zn in oxide form and Zn in metal form, respectively.[40] The fitting

Table 2. Details of the Fitting Parameters for XPS of O 1s and Zn 2p Core Level Spectra in Graphene−ZnO Hybrid Nanostructures[a]

	O 1s			Zn 2p			atomic percentage	
sample	peak 1 (eV)	peak 2 (eV)	A21	peak 1 (eV)	peak 2 (eV)	A21	O 1s (%)	Zn 2p (%)
GRZN1	529.9	531.03	1.84	1021.28	1021.67	0.54	70.3	29.7
GRZN2	529.23	530.12	2.32	1021.4	1022.07	0.44	67.1	32.9

[a]A21 denotes the ratio of integrated intensities of Peak 2 to Peak 1. Atomic percentage of O and Zn in various samples as determined from XPS data is shown for comparison.
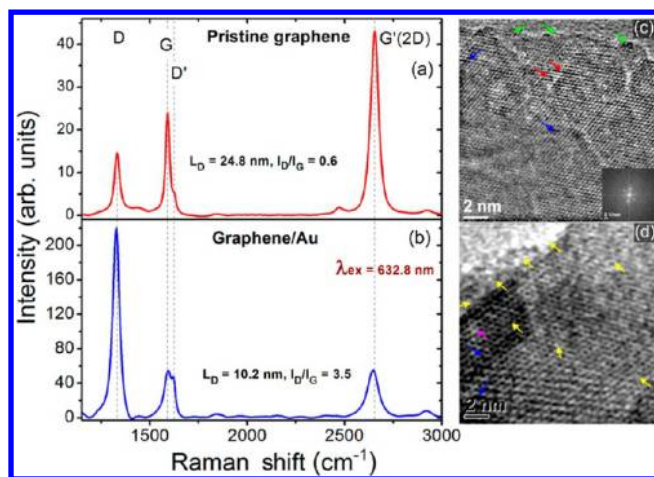
384

dx.doi.org/10.1021/am404411c | ACS Appl. Mater. Interfaces 2014, 6, 377−387

Figure 9. Evolution of characteristic Raman modes (D, G, D′, and G′ bands) of (a) pristine graphene and (b) after Au deposition on graphene. (c, d) Corresponding HRTEM images showing lattice defects. Hexagonal lattice spots of the single crystal graphene are shown in the inset of (c). Color arrows indicate various kinds of defects: green, edge defects; red, line defects; blue, vacancies; and yellow, Au clusters.

intense and sharp D band whose intensity is nearly equal to the G band, and this essentially implies a significant presence of in-plane defects in the graphene layer (Supporting Information, Figure S2).

We believe that, during the RTA treatment of the substrate at 600 °C in Ar atmosphere, Au atoms migrate and segregate at the defect sites to form Au clusters, and dewetting (liquid and solid) may be higher at the graphene defect sites. Indeed, we observe distinctly different behavior of Au clustering on the Si/SiO₂ substrate and Si/SiO₂/graphene substrates coated with a Au layer during the RTA process. Spherical Au nanoparticles are formed in the former case, while nonspherical or dumbbell-shaped bigger Au NPs are formed in the latter case (see Figure S3, Supporting Information). The increase in intensity of the D band as compared to that of the G band after Au deposition also indicates a plasmonic enhancement of the Raman intensity caused by preferential clustering of the Au atoms specifically at the defect sites in graphene. This provides a very important clue to the crucial role of defect sites on the graphene layer in the catalytic growth of highly aligned graphene−ZnO NR and NW hybrids. Recently, Wang et al. provided direct evidence of metal doping/clustering at the in-plane defect sites in graphene by in situ aberration-corrected TEM.[42] The stability of the metal clusters was argued on the basis of high binding energy of the metal−vacancy complex in graphene. Note that some of the Au atoms may diffuse through the graphene[43] and form chemical bonds with carbon atoms of graphene as longer Au−C bonds,[42] and this may be responsible for the dumbbell-shaped Au NPs (Figure S3, Supporting Information). Shape deformation and larger dimension of the Au NPs clearly indicate that a large number of Au atoms migrate and cluster preferentially at the defect sites, driven by the dewetting behavior of Au on the graphene layer[17] and for energy minimization. Due to the dewetting behavior of graphene, bigger size Au NPs form at the defect sites, and highly aligned ZnO NRs and NWs are formed at these sites depending on the density of Au NPs.

FESEM image analysis shows that areal density of Au NPs and ZnO NWs on the Si/SiO₂ substrate (without a graphene layer) is ~117 and 110 μm^{-2}, respectively. Thus, there is a one

to one correspondence between the density of ZnO NWs and the density of Au catalyst on the SiO₂ substrate. In the presence of a graphene layer, the areal density of Au NPs is reduced to ~25 μm^{-2} due to bigger size clusters, and ZnO NRs grown over it have a density of ~15 μm^{-2}. Thus, again there is a one to one correspondence between the density of ZnO NRs and the density of Au NPs grown on graphene. This reduced density of Au NPs on the graphene layer is dictated by the thickness and dewetting behavior of graphene and the density of defects in the graphene layer. Interestingly, Raman analysis shows that average areal density of defects in prinstine graphene and the graphene/Au hybrid layer is in the range 490−860 and 2860−5020 μm^{-2}, respectively. It implies a nearly six-fold increase in defect density after Au deposition by sputtering. Details of this analysis will be treated elsewhere. On the other hand, Au NP density is only about 5% of the graphene defect density, which is limited by the thickness of the Au layer deposited. Thus, the density of ZnO NRs and NWs is lower than the density of defects and density of Au NPs, as expected.

Further, we noticed a change in the binding energy and increase in the fwhm of the C 1s XPS spectrum of graphene before and after Au deposition on graphene (data not shown). This signifies a covalent bonding between foreign atoms and graphene[44] and structural disorder due to longer Au−C bond length than the C−C bond length in graphene.

Due to the higher sticking coefficient of ZnO with Au NPs and lower sticking coefficient with solid graphene,[15] Zn vapor droplets along with the oxygen migrate from the graphene surface toward the most favorable liquid Au droplets, and as a result vertically aligned ZnO NRs/NWs were formed by a self-catalytic VLS growth process. In the case of Au film on a graphene substrate, dense ZnO NWs grow due to the larger density of Au islands on graphene with smaller diameter that makes VLS growth of ZnO NWs with diameters less than 100 nm. Indeed, the VLS mechanism of growth is confirmed here from the presence of Au droplets on the tip of the ZnO NRs, as found from FESEM image of the NRs (Figure 3(e)). On the other hand, direct growth on the graphene substrate follows the vapor−solid (VS) mechanism because a large quantity of Zn migrates on the surface of the graphene with much less sticking coefficient, and a continuous supply of Zn leads to Zn adsorption followed by dewetting resulting in randomly oriented ZnO NRBs. Interestingly, the lattice mismatch between the hexagonal ZnO crystal and graphene bond centered sites is very low.[14] This could lead to epitaxial growth of ZnO NRs on graphene, and this is likely to be responsible for the growth of hexagonal faceted ZnO NRs in the presence of Au NP catalyst.[14,16] Munshi et al.[14] demonstrated epitaxial growth of vertically aligned GaAs NWs on few-layer graphene by the self-catalyzed VLS technique using a molecular beam epitaxy. Hong et al.[16] showed that high-quality graphene is critical for obtaining vertically well-aligned InAs NWs on the graphene substrate with strong van der Waals attraction. However, our results demonstrate that self-catalytic growth on the graphene layer in the absence of Au catalyst does not yield aligned ZnO NWs. It has been pointed out that the perfect epitaxial relation of Au(111) with graphene (002) forces the Au NPs to bind with the graphene layer and aids the growth process.[15] We believe that clear hexagonal facets of the as-grown ZnO NRs in the presence of graphene may be caused by the hexagonal arrangement of carbon atoms in the graphene lattice. During the growth, semiconductor atoms can absorb

385

dx.doi.org/10.1021/am404411c | ACS Appl. Mater. Interfaces 2014, 6, 377−387

above the center of the hexagonal carbon rings (H− site) or above the bridge between two carbon atoms (B− site), as discussed by Munshi et al.[14] Thus, the presence of Au catalyst directed the aligned growth of ZnO NRs, while the hexagonal carbon ring in graphene helps to attain a hexagonal facet of the ZnO NRs. Note that due to a relatively low temperature growth process adopted here, self-catalytic growth may be less efficient, and as a result, unreacted Zn and O remain in the final product. Nevertheless, the demonstration of graphene-assisted low-temperature growth of high-quality ZnO NRs and NWs on graphene is a significant step in the fabrication of integrated optoelectronic devices involving two powerful optical materials, namely, graphene and ZnO nanostructures. We believe these results will stimulate further investigations on the design and control of defects in graphene and low cost fabrication of the graphene−semiconductor NW array based novel hybrid devices with improved functionalities.

4. CONCLUSION

We have demonstrated single- and few-layer graphene as a versatile 2D platform for the growth of well-aligned 1D ZnO nanostructures such as NRs, NWs, and NRBs at a relatively low temperature and reported the optical properties of the graphene−ZnO NW/NR hybrids that are superior to previous reports. Systematic studies on the specific role of graphene and Au catalyst in the growth of highly aligned ZnO NRs and NWs were undertaken to understand the growth mechanism. It was revealed that the combined effect of the graphene and Au NPs leads to the formation of high-quality well-aligned ZnO NRs and NWs, while direct growth on the graphene substrate yielded randomly oriented ZnO NRBs. Detailed analysis involving HRTEM and Raman spectroscopy reveals the crucial role of in-plane defects in the pristine graphene and clustering of Au atoms at the defect sites on the growth of highly crystalline ZnO NRs/NWs with clear hexagonal facets. We believe that hexagonal-faceted ZnO NRs result from the epitaxial growth of NRs on the graphene bond centered sites, and Au NPs catalyze the vertical growth. Finally, PL studies on the as-grown and post-growth annealed graphene−ZnO NR, NW, and NRB hybrids show sharp UV emission that was substantially improved upon post-growth annealing at 500 °C. Several visible PL bands were identified from these hybrid nanostructures that are tentatively attributed to the intrinsic defects associated with the oxygen-rich growth conditions. Conclusions from PL analysis are fully supported by the XPS analysis. Our studies reveal the importance of defect engineering in graphene for low cost vapor-phase fabrication of novel graphene−semiconductor oxide NW hybrid based devices with newer and improved functionalities.

ASSOCIATED CONTENT

Ⓢ Supporting Information
FESEM image of the ZnO nanostructures grown on Si/SiO_2 substrate without the graphene and Au layers (Figure S1), Raman spectrum of pristine single layer graphene indicating in-plane defects on the layer (Figure S2), FESEM image of Au NPs on Si/SiO_2 and Si/SiO_2/graphene substrates after the RTA treatment (Figure S3), and the details of peak parameters used for fitting of the PL peaks with Gaussian line shapes (Table T1) are provided here. This material is available free of charge via the Internet at http://pubs.acs.org.

AUTHOR INFORMATION

Corresponding Author
*Tel.: +91 361 2582703. Fax: +91 361 2582749. E-mail: giri@ iitg.ernet.in.

Notes
The authors declare no competing financial interest.

REFERENCES

(1) Park, W. I.; Lee, C.-H.; Lee, J. M.; Kim, N.-J.; Yi, G.-C. *Nanoscale* **2011**, *3*, 3522−3533.
(2) Geim, A. K.; Novoselov, K. S. *Nat. Mater.* **2007**, *6*, 183−191.
(3) Nair, R. R.; Blake, P.; Grigorenko, A. N.; Novoselov, K. S.; Booth, T. J.; Stauber, T.; Peres, N. M. R.; Geim, A. K. *Science* **2008**, *320*, 1308.
(4) Lee, C.; Wei, X.; Kysar, J. W.; Hone, J. *Science* **2008**, *321*, 385− 388.
(5) Ghosh, S.; Calizo, I.; Teweldebrhan, D.; Pokatilov, E. P.; Nika, D. L.; Balandin, A. A.; Bao, W.; Miao, F.; Lau, C. N. *Appl. Phys. Lett.* **2008**, *92*, 151911−3.
(6) Balandin, A. A.; Ghosh, S.; Bao, W.; Calizo, I.; Teweldebrhan, D.; Miao, F.; Lau, C. N. *Nano Lett.* **2008**, *8*, 902−907.
(7) Chang, H.; Sun, Z.; Ho, K. Y.-F.; Tao, X.; Yan, F.; Kwok, W.-M.; Zheng, Z. *Nanoscale* **2011**, *3*, 258−264.
(8) Lee, J. M.; Yi, J.; Lee, W. W.; Jeong, H. Y.; Jung, T.; Kim, Y.; Park, W. I. *Appl. Phys. Lett.* **2012**, *100*, 061107−5.
(9) Dhara, S.; Giri, P. K. *J. Appl. Phys.* **2011**, *110*, 124317−9.
(10) Dutta, M.; Sarkar, S.; Ghosh, T.; Basak, D. *J. Phys. Chem. C* **2012**, *116*, 20127−20131.
(11) Dhara, S.; Giri, P. K. *J. Appl. Phys.* **2012**, *111*, 044320−7.
(12) Chan, M. H.; Chen, J. Y.; Lin, T. Y.; Chen, Y. F. *Appl. Phys. Lett.* **2012**, *100*, 021912−3.
(13) Cao, B. Q.; Zúñiga-Pérez, J.; Boukos, N.; Czekalla, C.; Hilmer, H.; Lenzner, J.; Travlos, A.; Lorenz, M.; Grundmann, M. *Nanotechnology* **2009**, *20*, 305701.
(14) Munshi, A. M.; Dheeraj, D. L.; Fauske, V. T.; Kim, D.-C.; van Helvoort, A. T. J.; Fimland, B.; Weman, H. *Nano Lett.* **2012**, *12*, 4570−4576.
(15) Kumar, B.; Lee, K. Y.; Park, H. K.; Chae, S. J.; Lee, Y. H.; Kim, S.-W. *ACS Nano* **2011**, *5*, 4197−4204.
(16) Hong, Y. J.; Lee, W. H.; Wu, Y.; Ruoff, R. S.; Fukui, T. *Nano Lett.* **2012**, *12*, 1431−1436.
(17) Ng, H. T.; Li, J.; Smith, M. K.; Nguyen, P.; Cassell, A.; Han, J.; Meyyappan, M. *Science* **2003**, *300*, 1249.
(18) Tam, N.-D.; Karandeep, S.; Meyyappan, M.; Michael, M. O. *Nanotechnology* **2012**, *23*, 194015.
(19) Dugaiczyk, L.; Ngo-Duc, T.-T.; Gacusan, J.; Singh, K.; Yang, J.; Santhanam, S.; Han, J.-W.; Koehne, J. E.; Kobayashi, N. P.; Meyyappan, M.; Oye, M. M. *Chem. Phys. Lett.* **2013**, *575*, 112−114.
(20) Kim, Y.-J.; Lee, J.-H.; Yi, G.-C. *Appl. Phys. Lett.* **2009**, *95*, 213101−3.
(21) Yin, Z.; Wu, S.; Zhou, X.; Huang, X.; Zhang, Q.; Boey, F.; Zhang, H. *Small* **2010**, *6*, 307−312.
(22) Park, H.; Chang, S.; Jean, J.; Cheng, J. J.; Araujo, P. T.; Wang, M.; Bawendi, M. G.; Dresselhaus, M. S.; Bulovic, V.; Kong, J.; Gradecak, S. *Nano Lett.* **2013**, *13*, 233−239.
(23) AbdulAlmohsin, S.; Cui, J. B. *J. Phys. Chem. C* **2012**, *116*, 9433− 9438.

(24) Choi, D.; Choi, M.-Y.; Choi, W. M.; Shin, H.-J.; Park, H.-K.; Seo, J.-S.; Park, J.; Yoon, S.-M.; Chae, S. J.; Lee, Y. H.; Kim, S.-W.; Choi, J.-Y.; Lee, S. Y.; Kim, J. M. *Adv. Mater. (Weinheim, Ger.)* **2010**, *22*, 2187−2192.

(25) Kim, Y.-J.; Hadiyawarman; Yoon, A.; Kim, M.; Yi, G.-C.; Liu, C. *Nanotechnology* **2011**, *22*, 245603.

(26) Lee, J. M.; Yi, J.; Lee, W. W.; Jeong, H. Y.; Jung, T.; Kim, Y.; Park, W. I. *Appl. Phys. Lett.* **2012**, *100*, 061107−5.

(27) Lin, J.; Penchev, M.; Wang, G.; Paul, R. K.; Zhong, J.; Jing, X.; Ozkan, M.; Ozkan, C. S. *Small* **2010**, *6*, 2448−2452.

(28) Ferrari, A. C.; Basko, D. M. *Nat. Nanotechnol.* **2013**, *8*, 235−246.

(29) Vanheusden, K.; Warren, W. L.; Seager, C. H.; Tallant, D. R.; Voigt, J. A.; Gnade, B. E. *J. Appl. Phys.* **1996**, *79*, 7983−7990.

(30) Lin, B.; Fu, Z.; Jia, Y. *Appl. Phys. Lett.* **2001**, *79*, 943−945.

(31) Janotti, A.; Van de Walle, C. G. *J. Cryst. Growth* **2006**, *287*, 58−65.

(32) Liu, J.; Soonil Lee, Y. H. A.; Park, J.-Y.; Koh, K. H. *J. Phys. D: Appl. Phys.* **2009**, *42*, 095401.

(33) Wang, M.; Zhou, Y.; Zhang, Y.; Kim, E. J.; Hahn, S. H. *Appl. Phys. Lett.* **2012**, *100*, 101906.

(34) Guo, B.; Qiu, Z. R.; Wong, K. S. *Appl. Phys. Lett.* **2003**, *82*, 2290−2292.

(35) Kohan, A. F.; Ceder, G.; Morgan, D.; Van de Walle, C. G. *Phys. Rev. B* **2000**, *61*, 15019−15027.

(36) Liao, Z.-M.; Zhang, H.-Z.; Zhou, Y.-B.; Xu, J.; Zhang, J.-M.; Yu, D.-P. *Phys. Lett. A* **2008**, *372*, 4505−4509.

(37) Li, D.; Leung, Y. H.; Djurisic, A. B.; Liu, Z. T.; Xie, M. H.; Shi, S. L.; Xu, S. J.; Chan, W. K. *Appl. Phys. Lett.* **2004**, *85*, 1601−1603.

(38) Willander, M.; Nur, O.; Bano, N.; Sultana, K. *New J. Phys.* **2009**, *11*, 125020.

(39) Asok, A.; Gandhi, M. N.; Kulkarni, A. R. *Nanoscale* **2012**, *4*, 4943−4946.

(40) Zhong, J.; Cheng, K.; Hu, B.; Gong, H.; Zhou, S.; Du, Z. *Mater. Chem. Phys.* **2009**, *115*, 799−803.

(41) Cançado, L. G.; Jorio, A.; Ferreira, E. H. M.; Stavale, F.; Achete, C. A.; Capaz, R. B.; Moutinho, M. V. O.; Lombardo, A.; Kulmala, T. S.; Ferrari, A. C. *Nano Lett.* **2011**, *11*, 3190−3196.

(42) Wang, H.; Wang, Q.; Cheng, Y.; Li, K.; Yao, Y.; Zhang, Q.; Dong, C.; Wang, P.; Schwingenschlögl, U.; Yang, W.; Zhang, X. X. *Nano Lett.* **2011**, *12*, 141−144.

(43) Gan, Y.; Sun, L.; Banhart, F. *Small* **2008**, *4*, 587−591.

(44) Kim, Y. A.; Fujisawa, K.; Muramatsu, H.; Hayashi, T.; Endo, M.; Fujimori, T.; Kaneko, K.; Terrones, M.; Behrends, J.; Eckmann, A.; Casiraghi, C.; Novoselov, K. S.; Saito, R.; Dresselhaus, M. *ACS Nano* **2012**, *6*, 6293−6300.

387

dx.doi.org/10.1021/am404411c | *ACS Appl. Mater. Interfaces* 2014, 6, 377−387